A Vertically Modularized Reconfigurable Wireless Power Transfer System: Architecture, Modeling, and Design

Huan Zhang, *Student Member, IEEE*, Yaoxia Shao, *Student Member, IEEE*, Ning Kang, *Student Member, IEEE*, Haojun Qin, *Student Member, IEEE*, Chengbin Ma, *Senior Member, IEEE*, and Ming Liu, *Senior Member, IEEE*

***Abstract*—It is known that megahertz (MHz) wireless power transfer (WPT) is particularly beneficial in terms of spatial freedom of power transfer and circuit compactness. Meanwhile, design complexity is a main obstacle to the spread of MHz WPT. In this article, a new modular design concept is proposed to conveniently reconfigure a MHz WPT system for different applications. Multiple predesigned functional unit modules can easily be combined to form a complete new WPT system with a different power level and transfer distance. A vertically stacked architecture is especially chosen to save space in actual applications. Detail analytical derivations are conducted to analyze the modular design, including the influence of different combinations of the unit modules. A new interleaved coil design is developed to reduce the proximity effect and cross coupling among the vertically stacked modules. Finally, the modular design concept is validated by experiments and demonstrates the desired scalability in both power levels and transfer distances. Through 15 combinations of the unit modules, the experimental WPT system can be reconfigured to provide an output power from 4 to 116 W. The effective transfer distance can be also extended from 30 to 90 mm and 80% system dc–dc efficiency is achieved within a 70-mm transfer distance using 100-mm-diameter printed circuit board coils.**

***Index Terms*—Megahertz (MHz), modular design, proximity effect, scalability, wireless power transfer (WPT).**

I. Introduction

WIRELESS power transfer (WPT) operating at multiple megahertz (MHz WPT) is a viable solution for transmitting a medium mount of power over a medium range. The MHz WPT is known to be especially advantageous in terms of the spatial freedom of power transfer and circuit compactness [1]. Meanwhile, mostly due to the obvious parasitics of the devices operating in the MHz bands, the parameter design of a high-performance MHz WPT system is usually not straightforward, requiring an intensive effort and long-time experience [2]. This design complexity is now a major obstacle to the spread of the MHz WPT despite the real needs for compactness and increased power transfer distance. It would be of interest, both for research or application, to develop a modular design, by which a new MHz WPT system can be conveniently reconfigured to meet different requirements for power level and transfer distance.

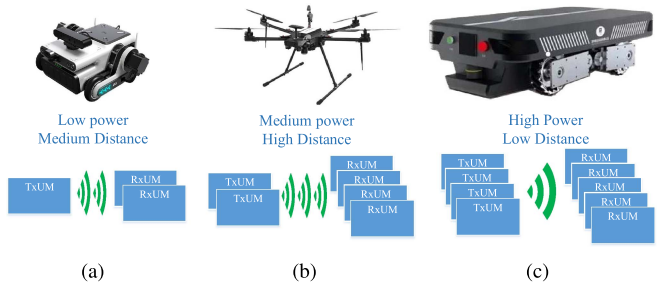

Fig. 1. Multiple MHz WPT applications with different power levels and transfer distances. (a) Small mobile robot. (b) Multirotor drone. (c) Automated guided vehicle.

As mentioned previously, in order to bring new scalability or reconfigurability, this article introduces the modular design concept into the MHz WPT. As illustrated in Fig. 1, based on this design concept, it is expected that multiple WPT applications with different requirements (e.g., output voltage, power level, and transfer distance) can be realized by different combinations of predesigned transmitting unit modules (Tx-UMs) and receiving unit modules (Rx-UMs). This modular architecture not only provides design flexibility, but also saves product development and maintenance costs. There are mainly three possible types of the modular architecture.

1) Modular converters: This architecture has been most widely discussed, in which multiple converter modules are connected either in parallel or series. The well-known full-bridge topology and push–pull/full-wave Class E topology are typical when applying this modular concept [3], [4], [5]. Guan et al. [6] use multiple modular converters to

Manuscript received 24 March 2022; revised 18 July 2022; accepted 13 September 2022. Date of publication 21 September 2022; date of current version 18 November 2022. This work was supported in part by the Power Electronics Science and Education Development Program of Delta Group, Natural Science Foundation of Shanghai under Grant 21ZR1431100, and in part by the National Natural Science Foundation of China under Grant 52277194 and Grant 52077132. Recommended for publication by Associate Editor M. Vitelli. *(Corresponding author: Ming Liu.)*

Huan Zhang, Yaoxia Shao, Ning Kang, Haojun Qin, and Chengbin Ma are with the University of Michigan-Shanghai Jiao Tong University Joint Institute/Global Institute of Future Technology, Shanghai Jiao Tong University, Shanghai 200240, China (e-mail: hzhang_93@sjtu.edu.cn; yaoxiashao@sjtu.edu.cn; corningkdc@sjtu.edu.cn; haojun.qin@sjtu.edu.cn; chbma@sjtu.edu.cn).

Ming Liu is with the Key Laboratory of Control of Power Transmission and Conversion of Ministry of Education and the School of Electronic Information and Electrical Engineering, Shanghai Jiao Tong University, Shanghai 200240, China (e-mail: mingliu@sjtu.edu.cn).

Color versions of one or more figures in this article are available at https://doi.org/10.1109/TPEL.2022.3208315.

Digital Object Identifier 10.1109/TPEL.2022.3208315

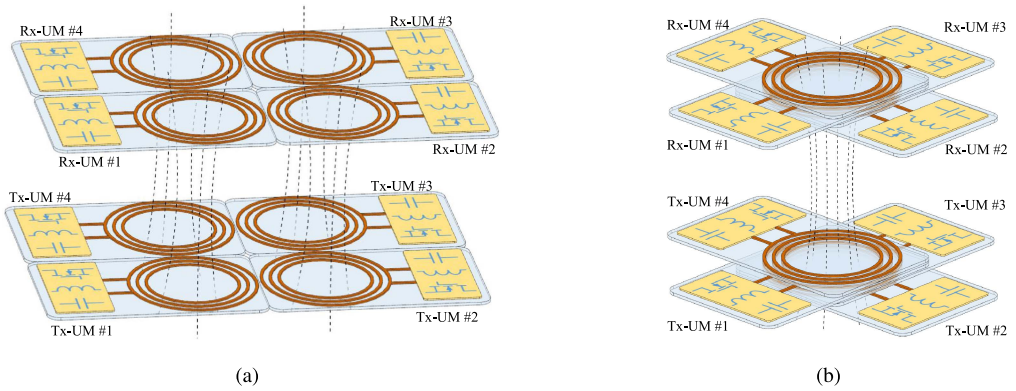

Fig. 2. Modular functional unit architecture. (a) Horizontally connected. (b) Vertically stacked.

achieve high-voltage conversion ratio. Control strategies and circuit topology optimization have been developed to suppress the circulation power [7], [8], [9]. Meanwhile, for the applications in WPT, the variations in the transfer distance or relative position of the coils make this architecture difficult to maintain a high system efficiency.

2) Modular coils: In this architecture, multiple transmitting coils and/or receiving coils are connected to a single inverter and/or rectifier, respectively. Wei et al. [10] discuss double-D and DDQ coil to reshape the magnetic route. Liu et al. [11] improve the effective transfer range of a WPT system by different positional combinations of unit module (UM) coils without using any control circuits or changes of resonant and matching capacitances. In [12], multiple modular repeating coils are used to improve the effective transfer distance. However, the power scalability of this modular-coil architecture is obviously limited by the designed capacity of the converters.

3) Modular functional units: Here, each UM consists of its own power converter (inverter or rectifier) and coupling coil, namely a fully functional WPT transmitter or receiver. In [13], the WPT system provides a high-efficiency 3-D power transfer based on a horizontally connected functional UMs, as shown in Fig. 2(a). This layout requires a relatively large area and only the Tx-UM modular design has been discussed. In [14], multiple UM coils using Litz wires were interwinded together to improve the system efficiency, and the coils are connected with their own inverters. Meanwhile, the interwinded coils make it difficult to reconfigure the WPT system.

In order to achieve a full scalability in power level and transfer distance, this article chooses the modular functional-unit architecture to implement reconfigurable WPT systems. Considering the limited space in most applications, especially for the receiving side, a new vertically connected architecture is proposed and developed [see Fig. 2(b)]. According to different requirements (e.g., output voltage, power level, and transfer distance), a final WPT system can be quickly configured through a specific combination of the standard UMs, both in transmitting and receiving sides. Therefore, this article is organized as follows: Section II discusses the vertically stacked UMs and their specific connections, detailed analytical derivations are conducted for modeling

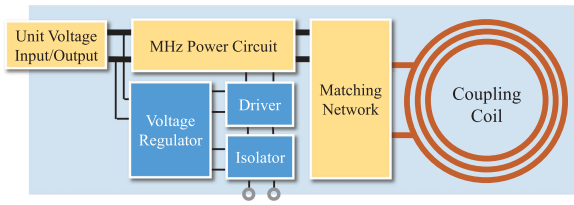

Fig. 3. Configuration of each functional UM.

and analysis purposes; Section III especially investigates the proximity effect of the conventional round coils and proposes a new interleaved coil design to reduce the proximity effect and cross-coupling among the UM coils; Section IV experimentally validates all the theoretical discussions and designs; and finally, Section V concludes this article.

II. Vertically Stacked Modular WPT System

A. Modular Architecture

Fig. 2(b) shows the basic architecture of a vertically stacked modular WPT system. Compared with the horizontal one in Fig. 2(a), this architecture stacks the functional UMs along the center of the coupling coils. Flexible reconfiguration of the WPT can be achieved in a compact space and with the scalability in power level and transfer distance.

As shown in Fig. 3, each functional UM includes a power converter (inverter or rectifier), a coupling coil (transmitting or receiving coil), driving and isolating circuits, namely a complete power transmitting/receiving functionality. All the Tx-UMs and Rx-UMs are vertically stacked to form a transmitter and receiver, respectively. By changing the combination of the Tx-UMs and Rx-UMs, the power level and transfer distance of a final system can be scaled, namely enabling a new reconfigurable WPT system.

Fig. 4 shows the 3-D models of the proposed reconfigurable WPT system comprising of 1–3 Tx-UMs and Rx-UMs. The Tx and Rx baseboards are used to mount multiple Tx-UMs and Rx-UMs. By mounting different numbers of UMs on the black baseboards, the WPT system can be flexibly reconfigured for different power levels and transfer distances. Generally, more Tx-UMs and Rx-UMs enable a higher power level and longer

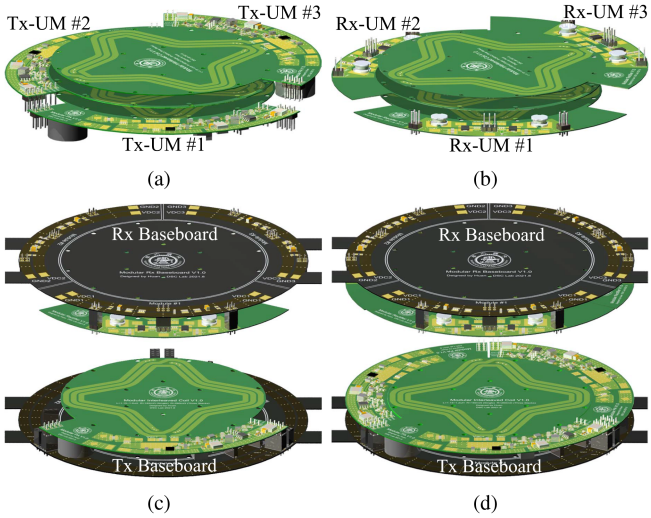

Fig. 4. 3-D models of the proposed vertically modularized reconfigurable WPT system. (a) Vertically stacked transmitter. (b) Vertically stacked receiver. (c) WPT system with one Tx-UM and one Rx-UM. (d) WPT system with three Tx-UMs and three Rx-UMs.

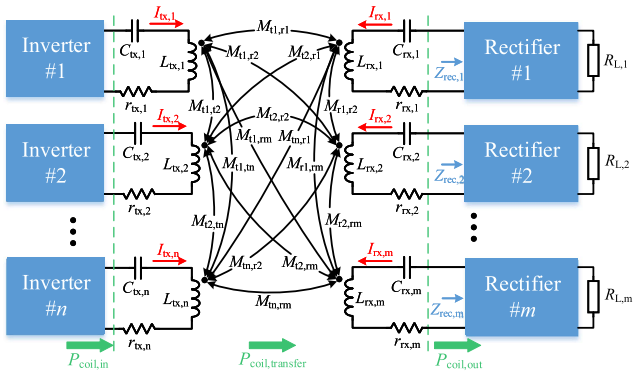

Fig. 5. Coupling condition of the proposed reconfigurable WPT system.

transfer distance, and vice versa. In this system, printed circuit boards (PCBs) are used to implement the UM coils because of their high consistency in coil size and shape. The thickness of PCB coils (0.8 mm in this article) is much smaller than the actual transfer distance (30∼90 mm in the final experiments). Thus, it is assumed that any pair of Tx and Rx UMs has the same transfer-coupling $M_{\rm tr}$.

B. Modeling and Analysis

Fig. 5 shows the coupling condition of a reconfigurable WPT system with n Tx-UMs and m Rx-UMs. Based on this model, the matrix of the voltages induced on the receiving coils, $\mathbf{U_{rx}}$, can be expressed as follows:

$$\mathbf{U_{rx}} = j\omega\mathbf{M_{tr}}\mathbf{I_{tx}} + j\omega\mathbf{M_{rr}}\mathbf{I_{rx}} \tag{1}$$

where $\mathbf{U_{rx}}$, $\mathbf{I_{tx}}$, and $\mathbf{I_{rx}}$ are the vectors of induced voltages and currents in transmitting coils and receiving coils, respectively. $\mathbf{M_{tr}}$ is the transfer coupling between transmitting and receiving coils and $\mathbf{M_{rr}}$ is the cross-coupling matrix of the receiving coils, which can be expressed as

$$\mathbf{M_{tr}} = \begin{bmatrix} M_{\rm t1,r1} & M_{\rm t2,r1} & \cdots & M_{\rm tn,r1} \\ M_{\rm t1,r2} & M_{\rm t2,r2} & \cdots & M_{\rm tn,r2} \\ \vdots & \vdots & \ddots & \vdots \\ M_{\rm t1,rm} & M_{\rm t2,rm} & \cdots & M_{\rm tn,rm} \end{bmatrix}$$

$$\mathbf{M_{rr}} = \begin{bmatrix} 0 & M_{\rm r1,r2} & \cdots & M_{\rm r1,rm} \\ M_{\rm r2,r1} & 0 & \cdots & \vdots \\ \vdots & \vdots & \ddots & M_{\rm rm,r(n-1)} \\ M_{\rm rm,r1} & \cdots & M_{\rm rm,r(n-1)} & 0 \end{bmatrix}. \tag{2}$$

Based on Ohm's law, the induced voltages can be also expressed as

$$\mathbf{U_{rx}} = -\mathbf{Z_R}\mathbf{I_{rx}} \tag{3}$$

where $\mathbf{Z}_R$ is the matrix of the receiver impedance. And the receiver impedance of the ith Rx-UM can be expressed as

$$Z_{\rm R,i} = r_{\rm rx,i} + j\omega L_{\rm rx,i} + \frac{1}{j\omega C_{\rm rx,i}} + Z_{\rm rec,i} \tag{4}$$

where $L_{\rm rx,i}$, $C_{\rm rx,i}$, and $r_{\rm rx,i}$ are the receiving coil inductance, compensation capacitance, and coil ac internal resistance of the ith Rx-UM, respectively. $Z_{\rm rec,i}$ is the equivalent ac load of the ith Rx-UM coil, which is equal to $R_{\rm rec,i} + jX_{\rm rec,i}$. Taking (3) into (1), the following equation can be obtained:

$$-\mathbf{Z_R}\mathbf{I_{rx}} - j\omega\mathbf{M_{rr}}\mathbf{I_{rx}} = j\omega\mathbf{M_{tr}}\mathbf{I_{tx}}. \tag{5}$$

Considering the high consistency of the PCB coils, the currents of the Rx-UMs can be assumed to be identical, i.e., $\dot{I}_{\rm rx,1} = \dot{I}_{\rm rx,2} = \cdots \dot{I}_{\rm rx,m}$, $R_{\rm rec,1} = R_{\rm rec,2} = \cdots R_{\rm rec}$. Thus, the ith receiver equivalent impedance $Z'_{\rm R,i}$ can be derived as follows, taking the influence of the cross coupling into account, namely matrix $\mathbf{M_{rr}}$ in (5):

$$Z'_{\rm R,i} = Z_{\rm R,i} + j\omega \sum_{k=1}^{k=m,k\neq i} M_{\rm ri,rk}. \tag{6}$$

In order to achieve a full resonance in the Rx-UMs, the resonance capacitor is

$$C_{\rm rx,i} = \frac{1}{\omega\left(\omega L_{\rm rx,i} + X_{\rm rec,i} + \omega \sum_{k=1}^{k=m,k\neq i} M_{\rm ri,rk}\right)}. \tag{7}$$

Based on the aforementioned derivations, the induced voltages on the transmitting side can be expressed as

$$\begin{aligned} \mathbf{U_{tx}} &= \omega^2\mathbf{M_{tr}}^{\rm T}(\mathbf{Z'_R})^{-1}\mathbf{M_{tr}}\mathbf{I_{tx}} + j\omega\mathbf{M_{tt}}\mathbf{I_{tx}} \\ &= \mathbf{Z_{ref}}\mathbf{I_{tx}} + j\omega\mathbf{M_{tt}}\mathbf{I_{tx}}. \end{aligned} \tag{8}$$

Here, $\mathbf{Z_{ref}}\mathbf{I_{tx}}$ represents the influence of the Rx-UMs to the Tx-UMs, in which $\mathbf{Z_{ref}}$ is the reflected impedance matrix. The term $j\omega\mathbf{M_{tt}}\mathbf{I_{tx}}$ represents the influence of the cross coupling between the Tx-UMs. Given a full resonance in Rx-UMs, the

reflected impedance matrix (i.e., the loading effect of the Rx-UMs on the Tx-UMs) can be further simplified as

$$\mathbf{Z_{ref}} = \omega^2 \mathbf{M_{tr}}^{\mathrm{T}} (\mathbf{Z'_R})^{-1} \mathbf{M_{tr}} = \frac{m \cdot \omega^2 {M_{\mathrm{tr}}}^2}{R_{\mathrm{rec}} + r_{\mathrm{rx}}} \begin{bmatrix} 1 & 1 & \cdots & 1 \\ 1 & 1 & 1 & \vdots \\ \vdots & 1 & \ddots & 1 \\ 1 & \cdots & 1 & 1 \end{bmatrix}_{n \times n}. \quad (9)$$

Note that there are certainly slight differences in the transfer coupling, i.e., $M_{\mathrm{ti,rj}}$'s. As mentioned in the aforementioned subsection, thanks to the high shape consistency and thin thickness (0.8 mm in this article) of the PCB coils, it can be assumed that the transfer coupling between each pair of Tx-UM and Rx-UM is identical, namely $M_{\mathrm{t1,r1}} = M_{\mathrm{t2,r3}} = \cdots = M_{\mathrm{tr}}$. Assuming again that the coil currents of the Tx-UMs are all identical ($\dot{I}_{\mathrm{tx,1}} = \dot{I}_{\mathrm{tx,i}} = \dot{I}_{\mathrm{tx}}$) and the cross coupling is fully compensated [15], the equivalent reflected impedance on each transmitting coil is pure resistive and can be expressed as

$$Z_{\mathrm{ref,i}} = R_{\mathrm{ref,i}} = \frac{U_{\mathrm{tx,i}}}{I_{\mathrm{tx}}} = \frac{mn \cdot \omega^2 M_{\mathrm{tr}}^2}{R_{\mathrm{rec}} + r_{\mathrm{rx}}}. \quad (10)$$

In Fig. 5, $P_{\mathrm{coil,in}}$ represents the total input ac power of Tx-UM coils; $P_{\mathrm{coil,out}}$ represents the total output ac power of Rx-UM coils. And the total transfer power $P_{\mathrm{coil,transfer}}$ from the transmitting side to the receiving side is

$$P_{\mathrm{coil,transfer}} = \sum_{i=1}^{n} \frac{I_{\mathrm{tx}}^2}{2} \mathrm{Re}\left(Z_{\mathrm{ref,i}}\right) = mn^2 \frac{(\omega M_{\mathrm{tr}})^2 I_{\mathrm{tx}}^2}{2\left(R_{\mathrm{rec}} + r_{\mathrm{rx}}\right)} = mn^2 P_{\mathrm{unit}} \quad (11)$$

where P_{unit} is the transfer power from one Tx-UM to one Rx-UM. It is determined by the mutual inductances between the transmitting and receiving coils, ac load of the receiving coils, and the transmitting coil currents. From the aforementioned equation, the total transfer power $P_{\mathrm{coil,transfer}}$ has a linear relationship with the Rx-UM number m and quadratic relationship with Tx-UM number n. Thus, compared with adding Rx-UMs, it is more effective to add Tx-UMs for a higher power transfer capability. Based on the aforementioned derivations, the coil efficiency of the WPT system comprising of n Tx-UM and m Rx-UM is derived as

$$\eta_{\mathrm{coil}} = \frac{P_{\mathrm{coil,out}}}{P_{\mathrm{coil,in}}} = \frac{P_{\mathrm{coil,transfer}}}{P_{\mathrm{coil,in}}} \frac{P_{\mathrm{coil,out}}}{P_{\mathrm{coil,transfer}}} = \frac{R_{\mathrm{ref}}}{R_{\mathrm{ref}} + r_{\mathrm{tx}}} \frac{R_{\mathrm{rec}}}{R_{\mathrm{rec}} + r_{\mathrm{rx}}} = \frac{nm\omega^2 M_{\mathrm{tr}}^2 R_{\mathrm{rec}}}{\left(r_{\mathrm{rx}} + R_{\mathrm{rec}}\right)\left(r_{\mathrm{rx}} r_{\mathrm{tx}} + R_{\mathrm{rec}} r_{\mathrm{tx}} + nm\omega^2 M_{\mathrm{tr}}^2\right)}. \quad (12)$$

Note the values of r_{rx} and r_{tx} are affected by the proximity effect between the stacked coils in the Rx-UMs and Tx-UMs. This important aspect will be further discussed in Section III.

According to (11) and (12), choosing the Rx-UM coil ac load (R_{rec}) also influences the system output power and efficiency.

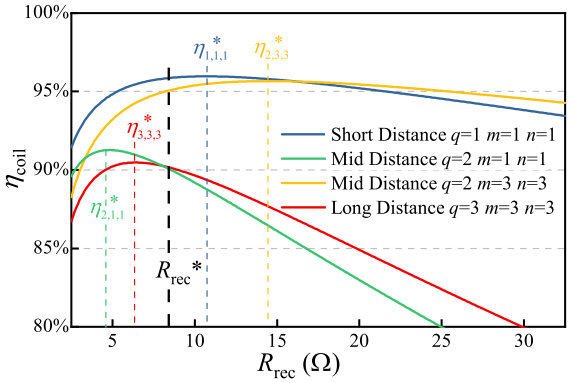

Fig. 6. Coil efficiency η_{coil} versus the Rx-UM coil ac load R_{rec}.

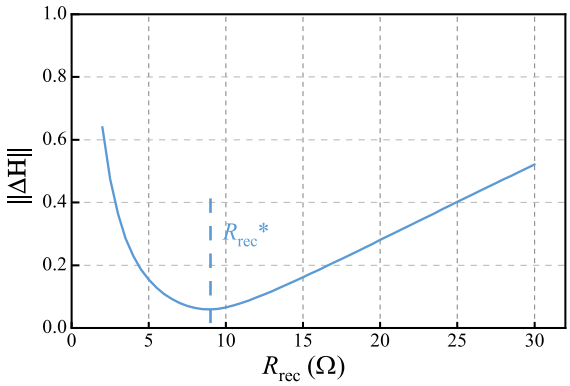

Fig. 7. Two-norm distance ($\|\Delta \mathbf{H}\|$) versus R_{rec}'s.

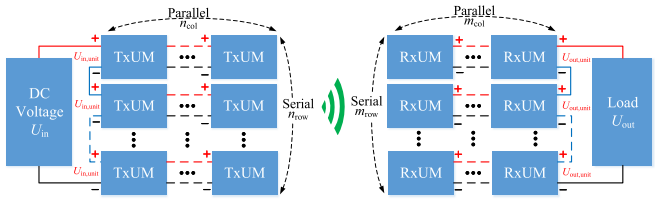

Fig. 8. Block-diagram of UM connections.

A smaller R_{rec} will enable a higher power output capability, while a too small R_{rec} may sacrifice the coil efficiency, as shown in Fig. 6. A target R_{rec} can be determine according to actual requirements, e.g., the ranges of targeted power level and transfer distance. It is generally desirable to maintain a relatively high coil efficiency under different scenarios, namely ${R_{\mathrm{rec}}}^*$ in Fig. 6.

Assuming that the target transfer range is divided into q parts, then based on (12), an ideal peak coil efficiency vector can be formulated, $\mathbf{H_{coil}}^* = \{\eta_{\mathrm{q,m,n}}{}^*\}$ (see the efficiency curves and their peaks in Fig. 6). Similarly, from (12), an actual coil efficiency vector $\mathbf{H_{coil}}(R_{\mathrm{rec}})$ can be analytically obtained. Then, an optimal ${R_{\mathrm{rec}}}^*$ is determined that minimizes the below 2-norm distance (see Fig. 7)

$$\min \|\Delta \mathbf{H}\| = \left\|\mathbf{H}_{\mathrm{coil}}\left(R_{\mathrm{rec}}\right) - \mathbf{H_{coil}}^*\right\|. \quad (13)$$

C. Influence of UM Connections

In order to ensure the power and voltage balances, all the UMs are connected in a symmetrical array, as shown in Fig. 8. In

the figure, n and m with different subscripts, "row" and "col," represent the serial and parallel numbers of Tx-UMs and Rx-UMs, i.e., $m = m_{\text{row}} m_{\text{col}}$, $n = n_{\text{row}} n_{\text{col}}$; U_{in} and U_{out} are the input and output voltages of the entire WPT system; and $U_{\text{in,unit}}$ and $U_{\text{out,unit}}$ are the unit input/output voltages of the power amplifier (PA) and rectifier.

Suppose $R_{\text{L,uint}}$ is the dc load of each Rx-UM, which is predesigned to fully use the capability of power devices. Thus, the impedance gain of each rectifier G_{rec} should be designed to match the required coil load ${R_{\text{rec}}}^*$, shown in (14). The design of G_{rec} will be discussed in Section IV-A.

$$ {R_{\text{rec}}}^* = G_{\text{rec}} R_{\text{L,unit}}. \tag{14} $$

Meanwhile, through different connections of the Rx-UMs, the final WPT system can achieve a different output power and voltage

$$ \frac{U_{\text{out}}^2}{P_{\text{out}}} = \frac{m_{\text{row}}}{m_{\text{col}}} R_{\text{L,unit}}. \tag{15} $$

In the transmitting side of the WPT system, a current source can be achieved through matching network design [16]. The peak current in each transmitting coil can be expressed as

$$ I_{\text{tx,i}} = \frac{U_{\text{in,unit}}}{G_{\text{pa}}} = \frac{U_{\text{in}}}{n_{\text{row}} G_{\text{pa}}} \tag{16} $$

in which G_{pa} reflects the relationship between the coil current in Tx-UM and dc input voltage of each Tx-UM. The value of G_{pa} is determined by inverter topology and impedance network, which will again be discussed in Section IV-A. From (14) to (16), the output/input voltage ratio can be calculated based on power balance as follows:

$$ \frac{U_{\text{out}}}{U_{\text{in}}} = m_{\text{row}} n_{\text{col}} \frac{\omega M_{\text{tr}} {R_{\text{rec}}}^* \sqrt{\eta_{\text{rec}}}}{\sqrt{2}\sqrt{G_{\text{rec}}} G_{\text{pa}} \left(r_{\text{rx}} + {R_{\text{rec}}}^*\right)} \tag{17} $$

in which η_{rec} represents the efficiency of the rectifier. If ${R_{\text{rec}}}^* \gg r_{\text{rx}}$, the voltage ratio can be further simplified and directly adjusted by a specific connection of UMs (m_{row} and n_{col}). The system output power can then be expressed as

$$ P_{\text{out}} = m n_{\text{col}}^2 \frac{\omega^2 {M_{\text{tr}}}^2 {R_{\text{rec}}}^* \eta_{\text{rec}}}{2 G_{\text{pa}}^2 (r_{\text{rx}} + {R_{\text{rec}}}^*)^2} U_{\text{in}}^2. \tag{18} $$

From (12), (17), and (18), the following conclusions can be made.

1) Increasing the number of UM helps improve the efficiency of the coil, which enhances the scalability in the transfer distance [refer to (12)].
2) A specific connection of a certain number of Rx-UMs only influences the output/input voltage ratio [refer to (17)].
3) The more Tx-UMs are connected in parallel, the greater the voltage output/input ratio and output power of the system [refer to (17) and (18)].
4) With the same number of Tx-UMs, the WPT system can achieve higher power output by adding more Rx-UMs [refer to (18)].

In addition, for a certain target transfer distance, the UMs with different connections can flexibly adjust the output power and voltage ratio to meet various practical needs. For instance, a reconfigurable WPT system with maximum three Tx-UMs and three Rx-UMs provides six different voltage ratios and nine different output power levels (fifteen voltage–power combinations in total). Those combinations will be verified in Table IV. At the same time, when choosing a specific combination, it is necessary to consider each UMs' voltage limit and power limit for protection purposes. Here, $U_{\text{tx,unit}}^{\max}$ ($U_{\text{rx,unit}}^{\max}$) is the maximum input (output) voltage for each Tx-UMs (Rx-UMs); and $P_{\text{tx,unit}}^{\max}$ ($P_{\text{rx,unit}}^{\max}$) is the maximum input (output) power for each Tx-UMs (Rx-UMs). They are both physically determined by a specific device (e.g., a MOSFET or diode). Then, below constraints need be considered in the system-level design.

$$ n_{\text{row}} \geq \frac{U_{\text{in}}}{U_{\text{tx,unit}}^{\max}}, \; m_{\text{row}} \geq \frac{U_{\text{out}}}{U_{\text{rx,unit}}^{\max}} $$
$$ n \geq \frac{P_{\text{out}}}{\eta_{\text{sys}} P_{\text{tx,unit}}^{\max}}, \; m \geq \frac{P_{\text{out}}}{P_{\text{rx,unit}}^{\max}}. \tag{19} $$

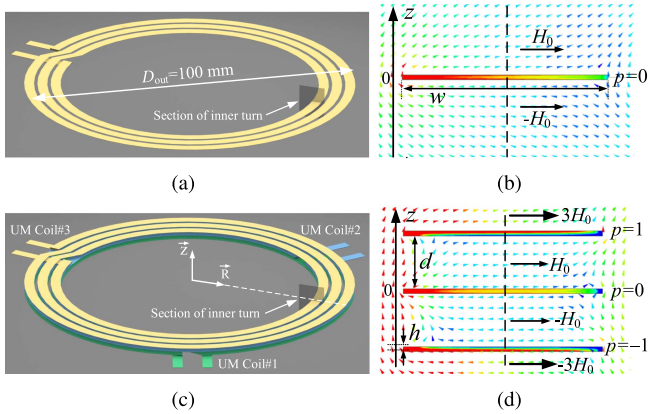

Fig. 9. Round UM coil models and simulation of current densities. (a) Single UM coil. (b) Inner turn current density of the single UM coil. (c) Vertically stacked three UM coils. (d) Inner turn current densities of three UM coils.

III. Interleaved Coil Design

In the existing WPT systems, the round coils are widely used because of the convenient features of isotropy and rotation symmetry. Fig. 9(a) shows a 3-D model of a three-turns round PCB coil. Here, the outer diameter of the coil (D_{out}) is 100 mm and the trace width w is 3 mm; the trace gap is 1 mm and the PCB trace thickness is 2 OZ ($h = 0.07$ mm). Based on this design, the coil can achieve relatively high quality factor at 6.78 MHz, i.e., $Q = 322$ here. However, when multiple UMs are stacked vertically, as shown in Fig. 9(c), the coil internal resistance r will rapidly increase because of the serious proximity effect at a high operation frequency, such as 6.78 MHz [17].

Table I shows the simulation results of the round-coil parameters in a single UM system and three-UMs system operating at 6.78 MHz. Here, L is coil inductance and k_{c} is cross-coupling coefficient between the Tx-UMs (or Rx-UMs). It is obvious that the internal resistances r's of the coils in the three UMs highly increase when comparing with r of the coil in the single UM. And r's of the three UMs are different. The values of the two

TABLE I
COIL PARAMETERS OF SINGLE UM AND THREE UMS

UM number \ UM type		Round Coil	Interleaved Coil
Single UM	L [μH]	1.44	1.24
	r [Ω]	0.19	0.18
	Q	322	280
Three UMs	L [μH]	1.42	1.21
	r [Ω]	[0.55, 0.35, 0.55]	[0.27, 0.28, 0.27]
	Q	[109, 172, 109]	[195, 190, 195]
	k_c	0.9	0.498

outer UMs are higher than that of the inner UM. This is because of the uneven distribution of the magnetic field strength, namely $3H_0$, H_0, $-H_0$, and $-3H_0$ from top to bottom in Fig. 9(d), and thus, higher current densities in the two outer UMs (i.e., higher r's).

The simulated current distributions in the sections of the inner turn coil are given in Fig. 9(b) and (d), analyzing the influence of the proximity effect in the vertically stacked coils. For the single UM WPT system, the current mainly concentrates on the inner edge of the trace, as shown in Fig. 9(b). This current distribution is jointly caused by the skin effect and proximity effect among the coil turns.

Since the trace width is usually much larger than the thickness, the magnetic field at the top and bottom surfaces of the single UM coil trace can be assumed to be in coil radial direction ($\overrightarrow{\mathrm{R}}$), and its amplitude is equal to H_0. When the three round UM coils are vertically stacked, as shown in Fig. 9(c), the magnetic field between the UM coils is still in radial direction, as shown in Fig. 9(d). According to the Ampere's circuital law, the magnetic field strength on the outer surfaces of the UM coils ($p = -1, p = 1$) is equal to $3H_0$. Here, the purpose of p is to number the UM coils for the convenience in the following magnetic field calculation. Taking these values as a boundary condition, the magnetic field strength inside the trace can be calculated by solving a 1-D Helmholtz equation [17]

$$\begin{cases} H_{\mathrm{R}} = H_1 e^{\gamma z} + H_2 e^{-\gamma z} \\ H_1 e^{\gamma[p(d+h)-h/2]} + H_2 e^{-\gamma[p(d+h)-h/2]} = (2p-1)\,H_0 \\ H_1 e^{\gamma[p(d+h)+h/2]} + H_2 e^{-\gamma[p(d+h)+h/2]} = (2p+1)\,H_0 \end{cases} \tag{20}$$

where γ is the propagation constant of the copper and d is the distance between two UM coils (equal to the thickness of the PCB). Then, the internal magnetic strength $H_{\mathrm{R}}(z)$ of each UM coil can be derived as

$$H_{\mathrm{R}}(z) = -H_0 \mathrm{csch}\,(h\gamma)\left\{(-1+2p)\sinh\left[\gamma\left(a-\frac{1}{2}h\right)\right] - (1+2p)\sinh\left[\gamma\left(a+\frac{1}{2}h\right)\right]\right\} \tag{21}$$

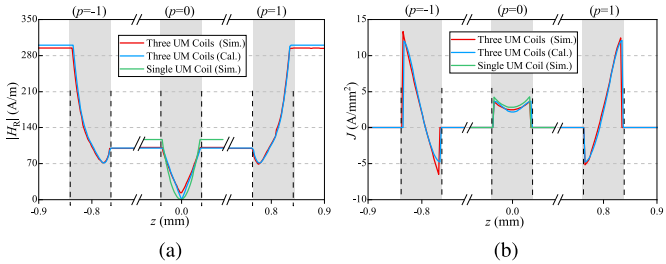

Fig. 10. Magnetic field strength and current densities in the single UM and three UMs. (a) Magnetic field strength H_{R}. (b) Current density J.

where $a = z - (d+h)p$. The current density inside the trace can thus be expressed by $J(z) = \frac{dH_{\mathrm{R}(z)}}{dz}$ as

$$J(z) = -\gamma H_0 \mathrm{csch}\,(\mathrm{h}\gamma)\left\{(-1+2\mathrm{p})\cosh\left[\gamma\left(\mathrm{a}-\frac{1}{2}\mathrm{h}\right)\right] - (1+2p)\cosh\left[\gamma\left(a+\frac{1}{2}h\right)\right]\right\}. \tag{22}$$

To verify the aforementioned two derived equations, Fig. 10 compares the simulation results and calculation results of the magnetic field strength $|H_{\mathrm{R}}|$ and current density J along the z direction represented by the dashed line in the middle of Fig. 9(b) and (d). The gray rectangles in Fig. 10 illustrate the thickness of the UM coils. In particular, the overlapping trace of the round UM coils greatly enlarge J at the top and bottom surfaces of the both outer UMs ($p = 1, p = -1$), as shown in Fig. 10(b). It is even worse that the proximity effect at a high frequency (6.78 MHz here) causes the coil current to partially reverse because of the closely stacked coils. With the same amount of total current, this negative current density naturally increases the positive current density. Power loss of the coil can be represented by

$$P_{\mathrm{loss}} = \frac{1}{2}\iiint_V \rho |J|^2 \mathrm{d}V \tag{23}$$

in which ρ is the resistivity of the PCB coils [18]. According to this equation, positive and negative current densities both result in power loss. Thus, compared with the inner coil ($p = 0$), the power loss of the two outer coils is increased. The more overlapping the UM coil traces, the larger magnetic strength around the coil surfaces. This in turn leads to more concentrated currents and higher power loss, and thus, enlarges the differences in parameters of the UM coils. In addition, the cross coupling (k_c) between the Tx-UMs (Rx-UMs) is very strong because of the overlapping traces in the vertically stacked coils. It enlarges the interference among the Tx-UM (or Rx-UM) coils and increases the voltage stress on the resonance capacitors (C_{tx} and C_{rx}).

To reduce the internal resistances of the UM coils, the differences in coil parameters, and the interference caused by the cross coupling, a novel interleaved UM coil design is proposed here, which largely avoids the overlap of UM coil traces, as shown in Fig. 11(a). This interleaved coil design effectively reduces the magnetic strength on the surfaces of the UM coils, and thus, coil internal resistances. Especially, the traces in the overlapping area are designed to be almost perpendicular to each

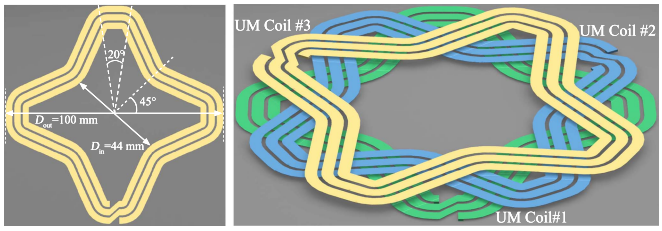

Fig. 11. Interleaved UM coil. (a) Single UM coil. (b) Three UM coils.

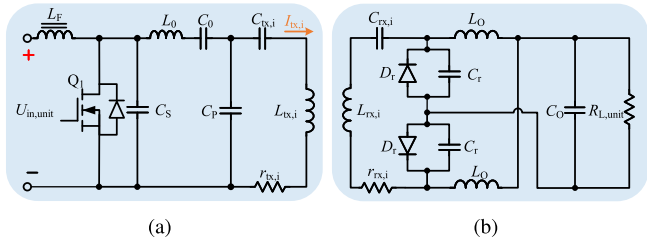

Fig. 13. Circuit topologies of Tx-UMs and Rx-UMs. (a) Class E PA and T-network in a Tx-UM. (b) Full-wave Class E rectifier in an Rx-UM.

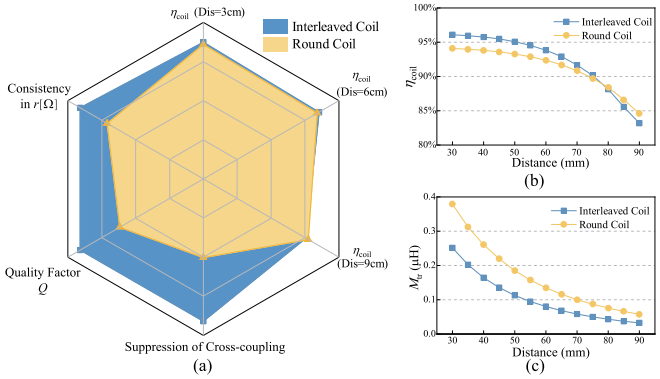

Fig. 12. Comparisons between round coil and interleaved coil designs in a three Tx-UMs three Rx-UMs WPT system. (a) Radar chart. (b) Coil efficiency η_{coil}. (c) Transfer coupling M_{tr}.

other [see Fig. 11(b)]. This further suppresses the influence of the proximity effect. In addition, the nonrotationally symmetrical design reduces the magnetic flux flowing among the UM coils, which greatly decreases the cross coupling k_{c} of UM coils.

The proposed interleaved coil design decreases the interference among the UMs, and thus, suppresses the circulating power among the Tx-UMs or Rx-UMs. As shown in Table I, compared with the conventional round coil, the internal resistances r and cross-coupling coefficient k_{c} of the interleaved UM coils are only about half of the round coil design in the three UMs. With this new interleaved design, the internal resistances of the three UMs are much closer to that of the single UM.

A comprehensive comparison between the round coil design and interleaved coil design in a WPT system with three Tx-UMs and three Rx-UMs is shown in Fig. 12(a). The advantages of the proposed interleaved coil design can then be summarized as follows:

1) reduced coil internal resistance, and thus, increased coil quality factor Q when multiple UMs are vertically stacked, namely with improved coil efficiency;
2) improved consistency of coil internal resistances that ensures the power balance among the Tx-UMs/Rx-UMs;
3) decreased cross coupling that suppresses the interference among the Tx-UMs/Rx-UMs and reduces the voltage stress of the coils and their compensation capacitors.

Fig. 12(b) compares the efficiencies of a three Tx-UMs three Rx-UMs system using the aforementioned two coil designs. In the majority of the transfer distances, the interleaved UM coils achieve a higher efficiency. But with a longer transfer distances (i.e., $D = 80 \sim 90$ mm), the round coil actually enables a higher efficiency. This is because that the special shape of interleaved UM coils sacrifices the effective transfer coupling, as shown in Figs. 11(b) and 12(c). The impact of this necessary sacrifice becomes especially obvious in a longer transfer distance.

Note that the rotation angle of 30° applies to three-UM configurations (Tx or Rx). This angle can be further reduced to accommodate more UMs, such as 22.5° for four UMs. The proposed interleaved coil design avoids overlapping traces of different UM coils as much as possible. However, the more UM coils still increase the proximity effect to some extent. Therefore, the actual number of UMs should be finalized to balance efficiency and output power.

IV. Experimental Setup and Results

A. Power Circuits

Fig. 13 shows power circuits of a Tx-UM and Rx-UM. The Tx-UM consists of a Class E PA, T-network, and Tx coil, as shown in Fig. 13(a). Here, the Class E topology is chosen because of its single-ended gate driving, zero-voltage switch (ZVS) operation and zero-voltage-derivation switching (ZVDS) operation [4]. And the T-network is designed to provide a close-to-constant current in the Tx-UM coil (i.e., a constant-current Class E PA), and thus, maintain a high PA efficiency under a varying transfer distance and different combinations of the UMs, thus determine G_{pa} [19], [20]. In the following experiments, GaN MOSFETs GS61004B (Q_1) are chosen as the PA switches because of their low switching and conduction losses in high-frequency operation. The chip IL711 is used to isolate the drive signal of each Tx-UM for a fully isolated UM design. The PA parameters and compensation capacitors $C_{\mathrm{tx,i}}$ are listed in Table II. The maximum input power of each Tx-UM ($P^{\max}_{\mathrm{tx,unit}}$) is 50 W and the maximum input voltage ($U^{\max}_{\mathrm{tx,unit}}$) is 30 V.

The Rx-UM consists of a full-wave Class E rectifier and an Rx coil, as shown in Fig. 13(b). The ac loads of Rx-UM coils $R_{\mathrm{rec,i}}$ can be designed by tuning the shunt capacitors C_{r} [5]. In the Rx-UMs, two Schottky diodes PDS3100 (D_{r}), which have high power capability and low forward voltage, are used for the rectification and $R_{\mathrm{L,unit}}$ is equal to 15 Ω. The circuit parameters of the Rx-UM are listed in Table II. The maximum output power of the Rx-UM ($P^{\max}_{\mathrm{rx,unit}}$) is 60 W and the maximum output voltage ($U^{\max}_{\mathrm{rx,unit}}$) is 30 V.

TABLE II
CIRCUIT PARAMETERS OF TX-UMS AND RX-UMS

Tx-UM Parameters					
L_F	C_S	L_0	C_0	C_P	G_{pa}
10 μH	168 pF	2.17 μH	362 pF	1170 pF	15.6
$C_{tx,i}$ [pF]					
1 Tx-UM	2 Tx-UMs		3 Tx-UMs		
500	362(#1), 362(#2)		247(#1), 247(#2), 247(#3)		
Rx-UM Parameters					
L_O	C_r	C_O	$R_{L,unit}$	$R_{rec}{}^*$	G_{rec}
10 μH	1410 pF	66 μH	15 Ω	8.5 Ω	0.57
$C_{rx,i}$ [pF]					
1 Rx-UM	2 Rx-UMs		3 Rx-UMs		
723	412(#1), 412(#2)		290(#1), 290(#2), 290(#3)		

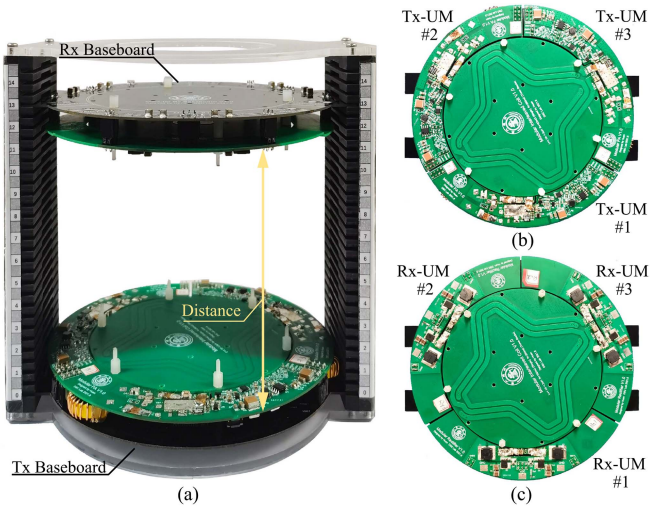

Fig. 14. Experimental setup. (a) System assembly. (b) Transmitter with three Tx-UMs. (c) Receiver with three Rx-UMs.

The voltage and power levels of Tx-UM and Rx-UM are mainly determined by the circuit topology and power components. Because of the Class E topology, input/output voltage V_{dc} and maximum switch voltage V_{SM} have a relationship of $V_{SM} \approx 3.56V_{dc}$[4]. Since the voltage rating of each power switch is 100 V, the maximum dc voltage of each UM is equal to 30 V. Then, the power levels of Tx-UMs and Rx-UMs are finalized based on the predefined maximum temperature (70 °C here) for a safe operation in a normal air flow.

B. System Setup and Signal Synchronization

Fig. 14 shows a vertically stacked reconfigurable WPT system operating at 6.78 MHz. This frequency is the lowest frequency in the globally recognized ISM (industrial, scientific, and medical) bands. It is the only frequency recommended by International Telecommunication Union Radiocommunication Sector for consumer device applications because it has minimal or nonexistent impact to other licensed bands [21].

The interleaved PCB coils, as discussed in Section III, are used in the Tx-UMs and Rx-UMs. The PCB thickness of each

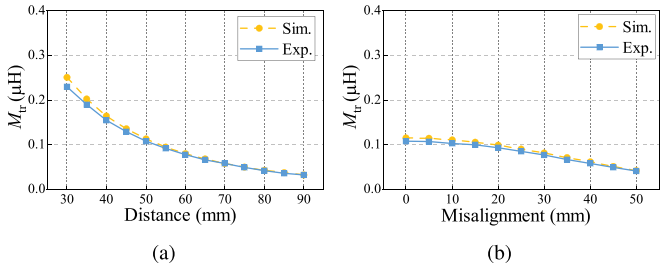

Fig. 15. Comparison of transfer-coupling M_{tr} in experiments (Exp.) and simulation (Sim.). (a) M_{tr} versus transfer distance. (b) M_{tr} versus misalignment.

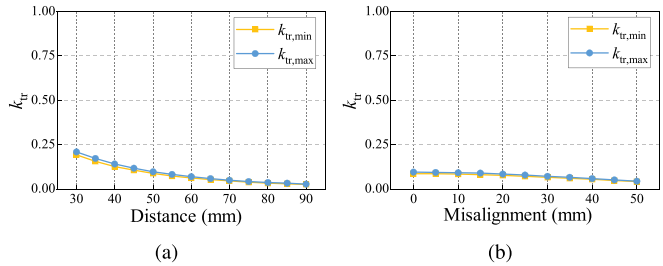

Fig. 16. Transfer coupling coefficient versus transfer distance and coil misalignment. (a) k_{tr} versus transfer distance. (b) k_{tr} versus coil misalignment.

TABLE III
CROSS-COUPLING OF INTERLEAVED UM COILS AND ROUND UM COILS

3 Stacked UM (PCB thickness=0.8 mm)	Interleaved UM Coils [μH]	Round UM Coils [μH]
$[M_{t1,t2}, M_{t1,t3}, M_{t2,t3}]$	[0.59, 0.58, 0.59]	[1.55, 1.43, 1.55]
$[M_{r1,r2}, M_{r1,r3}, M_{r2,r3}]$	[0.59, 0.58, 0.59]	[1.55, 1.43, 1.55]

UM is 0.8 mm. In the experiments, the transfer distance D varies from 30 to 90 mm, and different combinations of the UMs are adopted to validate the scalability of the reconfigurable WPT system. Each UM PCB is designed in a shape of a one third circle to achieve the $\pm 30^\circ$ rotation of interleaved UM coils, which makes full use of the space for a compact size.

Fig. 15 shows the experimental results of the transfer coupling M_{tr} of a single pair of the interleaved UM coils under different transfer distance and coil misalignment. Thanks to the high consistency between PCB coils and their 3-D models, the experimental and simulation M_{tr} are close to each other. Fig. 16 shows the variation ranges of the transfer coupling between different pairs of the Tx-UMs and Rx-UMs, in which $k_{tr,min}$ is the minimum transfer coupling coefficient ($k_{tr,min} = \frac{\min[M_{ti,rj}]}{L}$); and $k_{tr,max}$ is the maximum transfer coupling coefficient ($k_{tr,max} = \frac{\max[M_{ti,rj}]}{L}$). The closeness of the two curves in Fig. 16 validates the assumption of $M_{t1,r1} = M_{t2,r3} = \cdots = M_{tr}$ in (9).

The measurement results of the cross coupling M_{tt} (or M_{rr}) among the Tx-UMs (or Rx-UMs) are shown in Table III. It can be seen that the interleaved UM coils suppress the cross coupling more than two times compared with the round coils, which greatly decreases the power circulation and interference inside the Tx-UMs (or Rx-UMs). The difference in cross coupling is also small because of the interleaved UM coil design. Therefore,

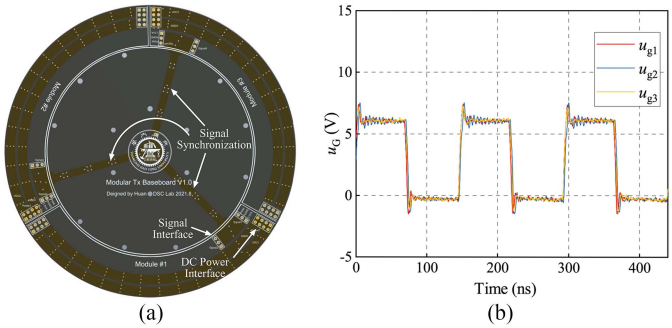

Fig. 17. Signal synchronization design. (a) Symmetrical driving signal design. (b) Driving signal u_G.

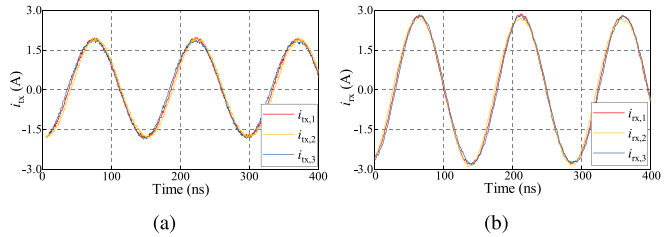

Fig. 18. Current waveforms of UM coils in three Tx-UMs and three Rx-UMs combination. (a) $I_{\mathrm{tx,i}}$. (b) $I_{\mathrm{rx,j}}$.

the same capacitance can be applied to compensate the cross coupling (refer to Table II).

Besides the power circuits and UM coils, the Tx and Rx baseboards are designed to provide the dc power interfaces and control signals of the UMs, as shown in Fig. 17(a). The UMs can be mounted on their respective baseboards to realize a flexible reconfiguration of the WPT system. Fig. 17(a) shows the symmetrical driving signal design on the Tx baseboard that helps achieve a better power balance among the UMs. Fig. 17(b) demonstrates well-aligned driving signals in the experiments. Fig. 18 shows the current waveforms of Tx-UM coils and Rx-UM coils. Thanks to the synchronized driving signals and high parameter consistency of the interleaved PCB coils, the currents in each Tx-UM ($i_{\mathrm{tx,i}}$) and Rx-UM ($i_{\mathrm{rx,j}}$) have similar phase and amplitude, which verifies the assumption of identical coil currents in Section II-B. And the amplitudes of $i_{\mathrm{tx,i}}$'s are 1.9 A under a 30-V dc input voltage of the constant current Class E PAs. This result validates the design of the PA voltage to current gain ($G_{\mathrm{PA}} = 15.6$) in (16).

C. Experimental Results

Fig. 19 shows the experimental results of the system output power. Here, the system input voltage U_{in} is 30 V and the Tx-UMs and Rx-UMs are connected in parallel ($m = m_{\mathrm{col}}$, $n = n_{\mathrm{col}}$). In Fig. 19, the red curve with square symbol ($n = 1, m = 1$) is a baseline output power $P_{\mathrm{out,unit}} = P_{\mathrm{unit}}\eta_{\mathrm{rx}}\eta_{\mathrm{rec}}$. The output power obtained by different numbers of UMs basically meets the relationship of $P_{\mathrm{out}}(m,n) = mn^2 P_{\mathrm{out,unit}}$, which validates (11). For instance, when the WPT system is consist of two Tx-UMs and one Rx-UM ($n = 2, m = 1, mn^2 = 4$), the output power (green curve with square symbol) maintains nearly four times of $P_{\mathrm{out,unit}}$ in different transfer distances. It can

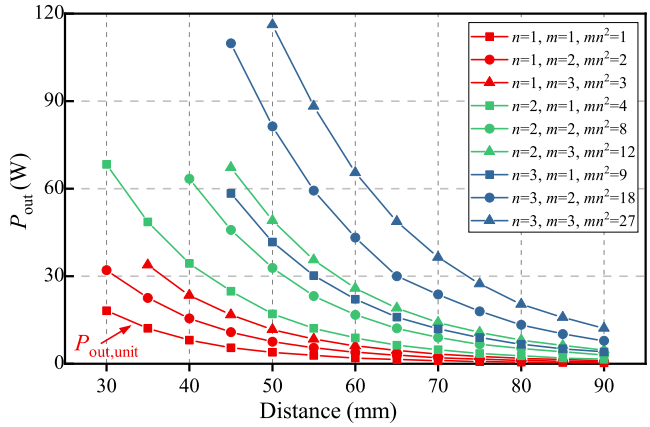

Fig. 19. System output power P_{out} versus transfer distance with different UM combinations.

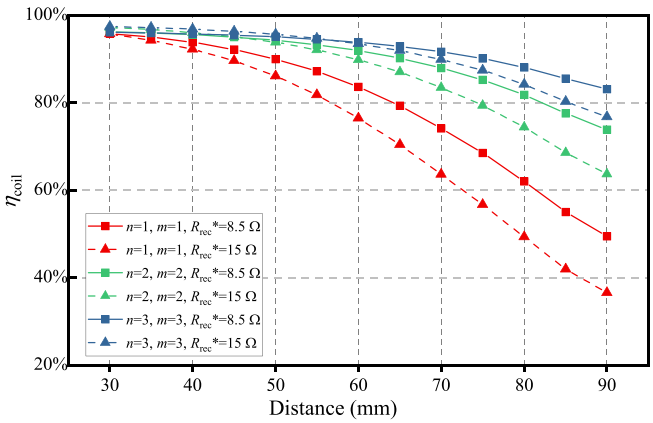

Fig. 20. Coil efficiency η_{coil} versus transfer distance under two different $R_{\mathrm{rec}}{}^*$s.

be seen that the output power is significantly improved by increasing the number of Tx-UMs and Rx-UMs, namely the power scalability of the proposed reconfigurable WPT system. The experimental results also show that increasing the number of the parallel connected Tx-UMs helps improve power capability, which can be explained by (11). And the maximum output power is 116 W, which is achieved at a 50-mm transfer distance by the three Tx-UMs and three Rx-UMs combination. Meanwhile, the system can also deliver about 110-W power in a 45-mm transfer distance with three Tx-UMs and two Rx-UMs combination, reflecting the scalability in transfer distance of the proposed reconfigurable WPT system. Note that the proposed modular design concept itself can be extended to applications requiring higher power levels, where power components with higher rated voltage, e.g., 650-V GaN MOSFETs, and larger PCB coil modules become necessary.

Fig. 20 shows the calculated coil efficiencies based on experimentally measured coil parameters with different $R_{\mathrm{rec}}{}^*$. According to the $R_{\mathrm{rec}}{}^*$ design discussed in Section II-B, $R_{\mathrm{rec}}{}^*$ is determined as 8.5 Ω in the experiments. And $R_{\mathrm{rec}}{}^* = 15\ \Omega$ (the optimal coil load for a specific scenario, $n = 3, m = 3$ and $D = 60$ mm) is chosen as a reference for comparison purposes. The 8.5 Ω $R_{\mathrm{rec}}{}^*$ clearly demonstrates an improved robustness of

TABLE IV
EXPERIMENTAL OUTPUT VOLTAGES AND POWERS WITH VARIOUS UM COMBINATIONS ($V_{\rm in} = 30$ V, $D = 50$ mm)

Tx-UM \ Rx-UM		$m_{\rm col}=1, m_{\rm row}=1$	$m_{\rm col}=2, m_{\rm row}=1$	$m_{\rm col}=3, m_{\rm row}=1$	$m_{\rm col}=1, m_{\rm row}=2$	$m_{\rm col}=1, m_{\rm row}=3$
$n_{\rm col}=1$ $n_{\rm row}=1$	Cal.	7.9 V, 4.2 W	7.9 V, 8.3 W	7.9 V, 12.5 W	15.8 V, 8.3 W	23.7 V, 12.5 W
	Exp.	7.8 V, 4.1 W	7.8 V, 8.1 W	7.8 V, 11.7 W	15.1 V, 7.6 W	23.3 V, 11.8 W
$n_{\rm col}=2$ $n_{\rm row}=1$	Cal.	15.8 V, 16.7 W	15.8 V, 33.4 W	15.8 V, 50.1 W	31.5 V, 33.4 W	47.3 V, 50.1 W
	Exp.	16.0 V, 17.0 W	15.7 V, 33.0 W	15.7 V, 49.3 W	31.4 V, 32.9 W	47.0 V, 49.1 W
$n_{\rm col}=3$ $n_{\rm row}=1$	Cal.	23.7 V 37.5 W	23.7 V, 75.1 W	23.7 V, 112.6 W	47.3 V, 75.1 W	71.0 V, 112.6 W
	Exp.	24.8 V, 41.0 W	24.5 V, 79.6 W	24.1 V, 116.2 W	47.5 V, 75.2 W	71.5 V, 113.6 W

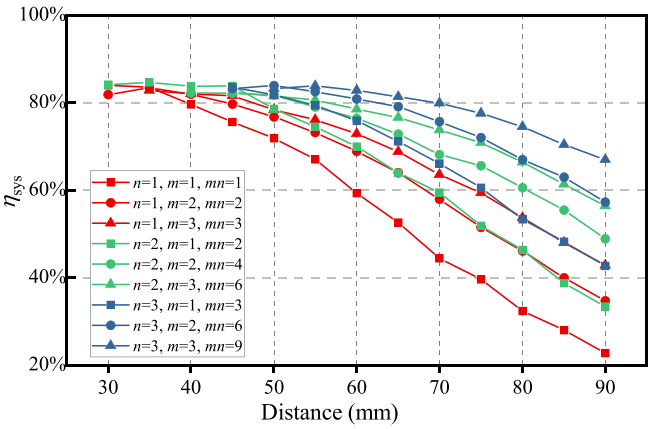

Fig. 21. System efficiency $\eta_{\rm sys}$ versus transfer distance with different UM combinations.

the coil efficiency against the variations in the transfer distance and UM combinations (see the solid curves).

The experimental results of the system dc–dc efficiency $\eta_{\rm sys}$ are shown in Fig. 21. It shows that the proposed reconfigurable system can always maintain over 80% dc–dc efficiency under different combinations of UMs and within a transfer distance of 30∼70 mm. The maximum efficiency is up to 85% and system efficiency can still achieve 67% at a 90-mm transfer distance using three Tx-UMs and three Rx-UMs. The maximum ratio of the transfer distance to coil diameter is about 0.9, and the minimum transfer-coupling coefficient is equal to 0.026. For conventional WPT systems, this coupling coefficient is too low to maintain a relative high efficiency. Thanks to the modular design, the effective transfer distance achieves great improvement without increasing the size of the coils, making it favorable for applications with strict space constraints. The modular design concept can also be used to update existing products without having to redesign the entire WPT system. This reflects the original design purpose of the reconfigurable WPT system, namely providing a high efficiency and scalability under different transfer distances and power levels.

Fig. 22 compares the calculation and experimental results. The power and voltage curves match the calculation results well, which verifies the accuracy of (17) and (18). Meanwhile, from (11), using more UMs can enlarge the output power. When the transfer power is high, the experimental coil efficiency curves are close to the calculated efficiency; while as the transfer power decreases, the differences between calculated and experimental efficiencies become larger. This is because the measurement error becomes apparent when the output power of each UM is small. Overall, (12) well reflects the effect of different numbers of UMs on the coil efficiency.

Table IV lists output voltages and powers with various UM combinations based on calculation (Cal.) and experiments (Exp.). Here, the input voltage $U_{\rm in}$ is 30 V and the transfer distance is 50 mm ($M_{\rm tr} = 108$ nH). It is obvious that there are six different output voltages $U_{\rm out}$ and nine different output power levels $P_{\rm out}$. Thus, the experimental reconfigurable WPT system can provide 15 different voltage–power combinations at a specific transfer distance, which can conveniently customize the WPT system for different applications. Compared with the calculated results, the experimental output power and voltage errors are less than 10%. Again, this verifies the accuracy of (17) and (18).

Fig. 23 shows the experimental results of the proposed reconfigurable system against misalignment of the Rx-UMs (distance = 50 mm). As same as the results with the changing transfer distance, the modular design can increase the output power and voltage when the coil misalignment is large. Again, the system dc–dc efficiency can also be largely improved when more UMs are used.

When multiple UM coils are stacked, it is difficult to measure the accurate value of the coil internal resistance. The system dc–dc efficiency is known to be related to the coil quality factor. For example, under the same transfer coupling $M_{\rm tr}$, the higher the efficiency, the higher the quality factor [22]. Fig. 24(a) shows the experimental efficiencies of the three Tx-UMs and three Rx-UMs reconfigurable system with conventional round coils and the proposed interleaved coils for various $M_{\rm tr}$. It is clear that, under the same $M_{\rm tr}$, the efficiency of the system with the interleaved coils is obviously higher than that of the system with the round coils. This result verifies the improvement of the quality factor Q in Fig. 12(a). Fig. 24(b) compares the system efficiencies under the same transfer distance. Same as Fig. 12(b), the system efficiency of the interleaved coil is lower in a long transfer distance ($D > 90$ mm), because the interleaved design sacrifices transfer coupling, but achieves the high parameter consistency.

Fig. 25 shows the input power $P_{\rm in,i}$ and output power $P_{\rm out,i}$ of each Tx-UM and Rx-UM in the reconfigurable WPT system ($m = m_{\rm col} = 3, n = n_{\rm col} = 3$). The interleaved coils are used as UM coils. With different transfer distances, the output power

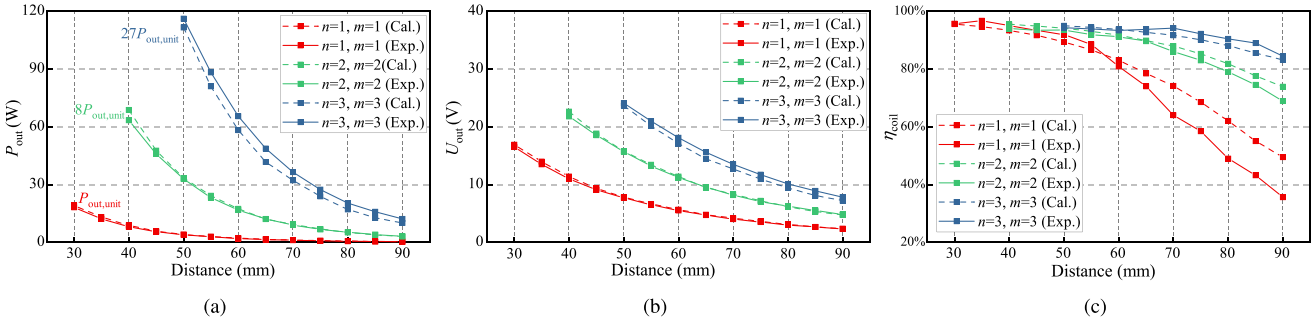

Fig. 22. Comparisons between calculation (Cal.) and experimental (Exp.) results against transfer distance. (a) $P_{\rm out}$. (b) $U_{\rm out}$. (C) $\eta_{\rm coil}$.

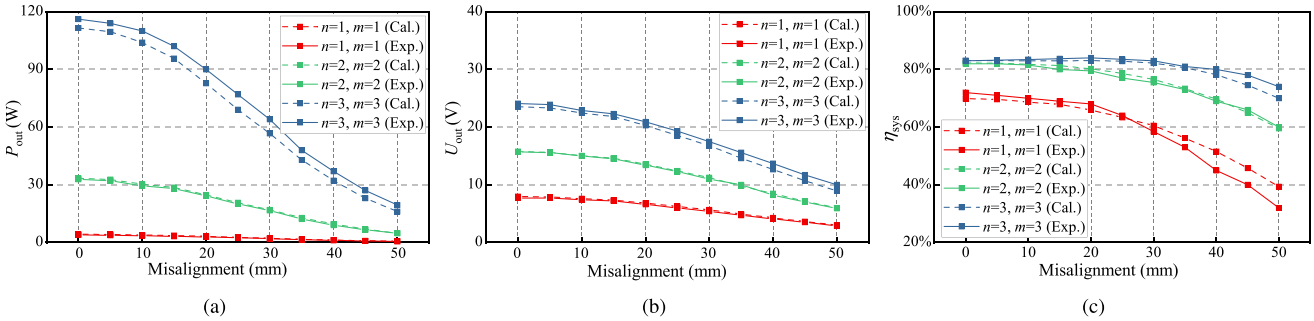

Fig. 23. Performance of the reconfigurable system against lateral misalignment (distance=50 mm). (a) $P_{\rm out}$. (b) $P_{\rm out}$. (c) $\eta_{\rm sys}$.

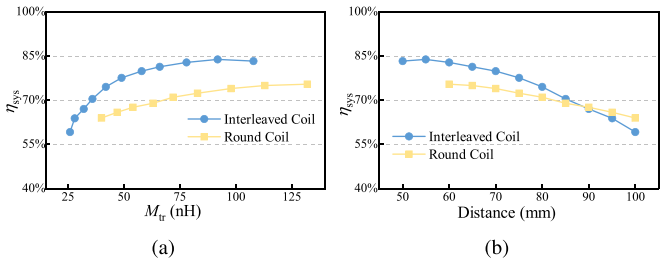

Fig. 24. Efficiency comparison between round UM coils and interleaved UM coils. (a) $\eta_{\rm sys}$ versus $M_{\rm tr}$. (b) $\eta_{\rm sys}$ versus distance.

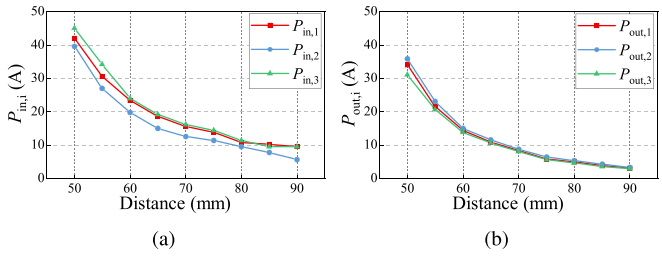

Fig. 25. Power balance among the UMs with the interleaved coils. (a) Input power $P_{\rm in,i}$ of Tx-UMs. (b) Output power $P_{\rm out,i}$ of Rx-UMs.

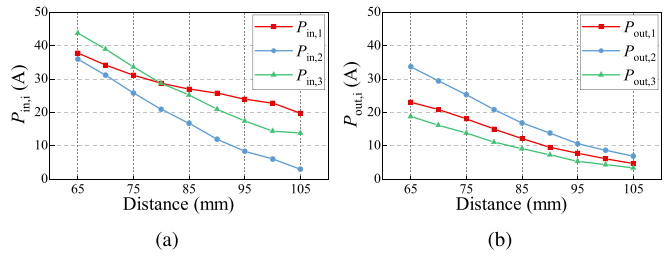

Fig. 26. Power balance among the UMs with the round coils. (a) Input power $P_{\rm in,i}$ of Tx-UMs. (b) Output power $P_{\rm out,i}$ of Rx-UMs.

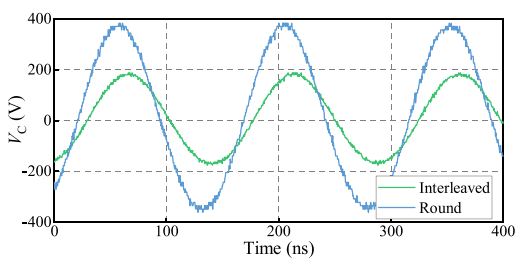

Fig. 27. Voltage across the Tx-UM resonance capacitor $C_{\rm tx}$.

$P_{\rm out,i}$ of each Rx-UMs achieves a high degree of consistency. Note that the input powers of the Tx-UMs, $P_{\rm in,i}$'s, are more different because of the natural deviations of the values of L_0's, the self-made inductors.

As a comparison, Fig. 26 shows the input/output powers of the reconfigurable WPT system using the conventional round coils (see Fig. 9). It is obvious that power differences are much larger than those using the interleaved ones. This result is mostly due to the inconsistent coil parameters (refer to Fig. 12(a) and Table I). The large cross coupling also reduces the values of the compensation capacitors ($C_{\rm tx}$ and $C_{\rm rx}$) by nearly half, and thus, makes the reconfigurable WPT system more sensitive to the capacitor manufacturing errors and circuit parasitics. The smaller compensation capacitance increases the voltage across the resonant capacitor $V_{\rm C}$, as shown in Fig. 27. This will place higher demands on power components and increase the cost per UM.

V. Conclusion

This article proposes and develops a vertically modularized reconfigurable WPT system, aiming at convenient implementation of MHz WPT in different applications. Detailed analytical derivations are conducted to model and analyze this new modular design of the MHz WPT systems. The influence of different UM connections is especially discussed to investigate the characteristics and design guideline under specific combinations of the UMs. A new interleaved coil design is then developed to reduce the proximity effect and cross coupling among the vertically stacked UMs. Finally, the proposed modular design concept is validated by experiments and newly demonstrates the desired scalability in both power levels (4∼116 W) and transfer distances (30∼90 mm). The system dc–dc efficiency maintains greater than 80% within a 70-mm transfer distance and reaches 67% in a 90-mm transfer distance using the 100-mm-diameter PCB UM coils.

References

[1] M. Pinuela, D. C. Yates, S. Lucyszyn, and P. D. Mitcheson, "Maximizing DC-to-load efficiency for inductive power transfer," *IEEE Trans. Power Electron.*, vol. 28, no. 5, pp. 2437–2447, May 2013.

[2] M. Liu, H. Zhang, Y. Shao, J. Song, and C. Ma, "High-performance megahertz wireless power transfer: Topologies, modeling, and design," *IEEE Ind. Electron. Mag.*, vol. 15, no. 1, pp. 28–42, Mar. 2021.

[3] J. Choi, D. Tsukiyama, and J. Rivas, "Comparison of SiC and eGaN devices in a 6.78 MHz 2.2 kW resonant inverter for wireless power transfer," in *Proc. IEEE Energy Convers. Congr. Expo.*, 2016, pp. 1–6.

[4] M. K. Kazimierczuk and D. Czarkowski, *Resonant Power Converters*. New York, NY, USA: Wiley, 2012.

[5] M. Liu, M. Fu, and C. Ma, "Low-harmonic-contents and high-efficiency class E full-wave current-driven rectifier for megahertz wireless power transfer systems," *IEEE Trans. Power Electron.*, vol. 32, no. 2, pp. 1198–1209, Feb. 2017.

[6] Y. Guan, C. Cecati, J. M. Alonso, and Z. Zhang, "Review of high-frequency high-voltage-conversion-ratio DC–DC converters," *IEEE J. Emerg. Sel. Topics Ind. Electron.*, vol. 2, no. 4, pp. 374–389, Oct. 2021.

[7] Q. Deng, P. Sun, W. Hu, D. Czarkowski, M. K. Kazimierczuk, and H. Zhou, "Modular parallel multi-inverter system for high-power inductive power transfer," *IEEE Trans. Power Electron.*, vol. 34, no. 10, pp. 9422–9434, Oct. 2019.

[8] A. Zhu et al., "Modeling and phase synchronization control of high-power wireless power transfer system supplied by modular parallel multi-inverters," *IEEE Trans. Veh. Technol.*, vol. 70, no. 7, pp. 6450–6462, Jul. 2021.

[9] Q. Deng, J. Liu, D. Czarkowski, W. Hu, and H. Zhou, "An inductive power transfer system supplied by a multiphase parallel inverter," *IEEE Trans. Ind. Electron.*, vol. 64, no. 9, pp. 7039–7048, Sep. 2017.

[10] G. Wei, J. Feng, J. Zhang, C. Wang, C. Zhu, and S. Yurievich Ostanin, "An efficient power and data synchronous transfer method for wireless power transfer system using double-D coupling coil," *IEEE Trans. Ind. Electron.*, vol. 68, no. 11, pp. 10643–10653, Nov. 2021.

[11] Z. Liu, Z. Chen, J. Li, and H. Zhao, "A shape-reconfigurable modularized wireless power transfer array system for multipurpose wireless charging applications," *IEEE Trans. Antennas Propag.*, vol. 66, no. 8, pp. 4252–4259, Aug. 2018.

[12] Y. Guan, Y. Xiao, Y. Cui, and D. Xu, "Analysis and optimal design of mid-range WPT system based on multiple repeaters," *IEEE Trans. Ind. Appl.*, vol. 58, no. 1, pp. 1092–1100, Jan./Feb. 2022.

[13] N. Kang, Y. Shao, M. Liu, and C. Ma, "Analysis and implementation of 3D magnetic field shaping via a 2D planar transmitting coil array," *IEEE Trans. Power Electron.*, vol. 37, no. 1, pp. 1172–1184, Jan. 2022.

[14] H. Zhou et al., "Input-series output-equivalent-parallel multi-inverter system for high-voltage and high-power wireless power transfer," *IEEE Trans. Power Electron.*, vol. 36, no. 1, pp. 228–238, Jan. 2021.

[15] M. Fu, T. Zhang, X. Zhu, P. C.-K. Luk, and C. Ma, "Compensation of cross coupling in multiple-receiver wireless power transfer systems," *IEEE Trans. Ind. Inform.*, vol. 12, no. 2, pp. 474–482, Apr. 2016.

[16] S. Liu, M. Liu, S. Yang, C. Ma, and X. Zhu, "A novel design methodology for high-efficiency current-mode and voltage-mode class-E power amplifiers in wireless power transfer systems," *IEEE Trans. Power Electron.*, vol. 32, no. 6, pp. 4514–4523, Jun. 2017.

[17] M. K. Kazimierczuk, *High-Frequency Magnetic Components*. New York, NY, USA: Wiley, 2009.

[18] B. S. Guru and H. R. Hiziroglu, *Electromagnetic Field Theory Fundamentals*. Cambridge, U.K.: Cambridge Univ. Press, 2009.

[19] X. Qu, Y. Jing, H. Han, S. Wong, and C. K. Tse, "Higher order compensation for inductive-power-transfer converters with constant-voltage or constant-current output combating transformer parameter constraints," *IEEE Trans. Power Electron.*, vol. 32, no. 1, pp. 394–405, Feb. 2017.

[20] Y. Shao, H. Zhang, M. Liu, and C. Ma, "Explicit design of impedance matching networks for robust MHz WPT systems with different features," *IEEE Trans. Power Electron.*, vol. 37, no. 9, pp. 11382–11393, Sep. 2022.

[21] International Telecommunication Union (ITU), General Aspects of Digital Transmission Systems–Terminal Equipments. Pulse Code Modulation of Voice Frequencies, International Telecommunication Union, Geneva, Switzerland, ITU-T Recommendation G, vol. 711, 2013.

[22] Q. Deng et al., "Frequency-dependent resistance of litz-wire square solenoid coils and quality factor optimization for wireless power transfer," *IEEE Trans. Ind. Electron.*, vol. 63, no. 5, pp. 2825–2837, May 2016.

Huan Zhang (Student Member, IEEE) received the B.S. degree in electrical engineering, in 2016, from Shandong University, Jinan, China, and the M.S. degree in electrical engineering, in 2019, from Shanghai Jiao Tong University, Shanghai, China, where he is currently working toward the Ph.D. degree in electrical and computer engineering with the University of Michigan–Shanghai Jiao Tong University Joint Institute.

His research interests include high-frequency power electronics and its applications in megahertz wireless power transfer and energy routers.

Mr. Zhang was the recipient of the Top ten First Stage Proposal Award at the Inaugural IEEE Global Student Wireless Power Competition in 2022, and the Best Paper Award at the IEEE Energy Conversion Congress and Exposition-Asia in 2020.

Yaoxia Shao (Student Member, IEEE) received the B.S. degree in mechanical design, manufacturing, and automation, with National Scholarship Honors, from Tongji University, Shanghai, China, in 2018. He is currently working toward the Ph.D. degree in electrical and computer engineering with the University of Michigan-Shanghai Jiao Tong University Joint Institute, Shanghai Jiao Tong University, Shanghai.

His research interests include high-frequency power conversion circuits and applications in both inductive power transfer and microwave power transfer.

Mr. Shao was the recipient of the Top ten First Stage Proposal Award at the Inaugural IEEE Global Student Wireless Power Competition in 2022, and the Best Paper Award at the IEEE Energy Conversion Congress and Exposition-Asia in 2020.

Ning Kang (Student Member, IEEE) received the B.S. degree in information engineering with National Scholarship Honors from the Nanjing University of Aeronautics and Astronautics, Nanjing, China, in 2017. He is currently working toward the Ph.D. degree in electrical and computer engineering with the University of Michigan-Shanghai Jiao Tong University Joint Institute, Shanghai Jiao Tong University, Shanghai, China.

His research interests include design and control strategies of megahertz wireless power transfer systems, such as multiple-transmitter systems under field programmable gate array high-speed control.

Haojun Qin (Student Member, IEEE) received the B.S. degree in automation from Wuhan University, Wuhan, China, in 2020. He is currently working toward the Ph.D. degree in electrical and computer engineering with the University of Michigan-Shanghai Jiao Tong University Joint Institute, Shanghai Jiao Tong University, Shanghai, China.

His research interests include multiport dc–dc converter and its control strategies.

Chengbin Ma (Senior Member, IEEE) received the B.S. degree in industrial automation from the East China University of Science and Technology, Shanghai, China, in 1997, and the M.S. and Ph.D. degrees in electrical engineering from The University of Tokyo, Tokyo, Japan, in 2001 and 2004, respectively.

From 2004 to 2006, he was an R&D Researcher with the Servo Motor Laboratory, FANUC Limited, Japan. Between 2006 and 2008, he was a Postdoctoral Researcher with the Department of Mechanical and Aeronautical Engineering, University of California, Davis, CA, USA. In 2008, he joined the University of Michigan-Shanghai Jiao Tong University Joint Institute, Shanghai Jiao Tong University, Shanghai, where he is currently a Professor of electrical and computer engineering. His research interests include battery and energy management, wireless power transfer, dynamics and motion control, and wide applications in electronic devices, electric vehicles, microgrids, smart grids, etc.

Dr. Ma was the recipient of many teaching and research awards at Shanghai Jiao Tong University, such as Teaching and Education Award in 2020 and Koguan Top Ten Best Teacher Award in 2017. He was also the recipient of Research Excellence Award from AirFuel Alliance, USA, in 2019. He is an Associated Editor for the IEEE TRANSACTIONS ON INDUSTRIAL INFORMATICS and IEEE JOURNAL OF EMERGING AND SELECTED TOPICS IN INDUSTRIAL ELECTRONICS. He served as Delegate of Energy Cluster (2019–2020), and is currently the Chair of Shanghai Chapter, IEEE Industrial Electronics Society.

Ming Liu (Senior Member, IEEE) received the B.S. degree in mechatronic engineering from Sichuan University, Sichuan, China, in 2007, and the Ph.D. degree in electrical and computer engineering from the University of Michigan-Shanghai Jiao Tong University Joint Institute, Shanghai Jiao Tong University, Shanghai, China, in 2017.

From 2017 to 2020, he was a Postdoctoral Research Fellow with the Department of Electrical Engineering, Princeton University, Princeton, NJ, USA. He joined the School of Electronic Information and Electrical Engineering, Shanghai Jiao Tong University, Shanghai, China, in 2020, where he is currently an Associate Professor of electrical engineering. His research interests include megahertz wireless power transfer, battery management systems, and high-frequency high performance power electronics for emerging applications.

Dr. Liu was the recipient of Top Ten Academic Star Award and Excellent PhD Thesis Award Nomination from Shanghai Jiao Tong University in 2016 and 2018, Research Excellence Award from AirFuel Alliance, USA, in 2019, and Best Paper Award of IEEE Energy Conversion Congress and Exposition—Asia in 2020. He was a Guest Editor for IEEE TRANSACTIONS ON INDUSTRIAL INFORMATICS and serves as the Chair for the Wireless Power Transfer for Energy Storage Charging Subcommittee of Energy Storage Technical Committee, IEEE Industrial Electronics Society.